Engineering Analysis with Boundary Elements 150 (2023) 353–363

Contents lists available at ScienceDirect

Engineering Analysis with Boundary Elements

journal homepage: www.elsevier.com/locate/enganabound

A point particle source model for conjugate heat and mass transfer in dispersed two-phase flows by BEM based methods

T. Gomboc *, J. Iljaž, J. Ravnik, M. Hriberšek

Faculty of Mechanical Engineering, University of Maribor, Smetanova 17, SI-2000 Maribor, Slovenia

ARTICLE INFO

Keywords:
Boundary Domain Integral Method
Dispersed two-phase flow
Two-way coupling
Spherical porous particle
Drying

ABSTRACT

The paper reports on development of a Boundary Element Method (BEM) based two phase dispersed flow model, that allows an accurate and efficient heat and mass transfer coupling by using a moving point source model to account for particle–fluid interaction. The two-way coupling model highlights the efficient use of the elliptic fundamental solution and the Dirac delta distribution properties to accurately evaluate the heat and mass point particle source impact on the continuous phase, solved by the Boundary Domain Integral Method (BDIM). In addition to the BDIM model of the particle–fluid heat and mass transfer interaction, the two-phase flow case under consideration is extended to the case of porous spherical particle drying with internal moving drying front, which is solved by the Boundary Element Method. As the two-phase flow is considered to be dilute, the particle–fluid momentum exchange is covered by a one-way coupling algorithm, with Lagrangian particle tracking used for determination of particle positions and velocities in the flow. Two computational cases are presented, where 1000 and 10000 particles are dried in a stream of hot air. Comparison between the obtained drying times for the cases of the one-way and the two-way heat and mass transfer coupling results shows, that the developed two-way coupling model accurately captures the effect of moisture accumulation and temperature decrease in the fluid phase, leading to realistic computations of drying rates of particles in the flow.

1. Introduction

In the process and environmental technology multiphase flows are very common, especially in the form of dispersed two-phase flows, as dispersion of particles ensures a high surface area of the particulate phase, leading to significant increase of heat and mass transfer rates between the phases. This is especially true in the case of drying applications, which are considered here as an application example, and cover spray dryers, fluid bed dryers, pneumatic dryers, among others.

Flows with particles can be dense or dilute. Modeling of dense particle two-phase flows is usually done in the Eulerian frame of reference for both phases, with governing equations for both phases derived based on volume averaging technique [1]. On the other hand, if we focus on dispersed flows with low mass loadings, as occur for example in spray or pneumatic dryers, the most appropriate approach is through the Euler–Lagrange description, with Eulerian frame used for the continuous phase and Lagrangian frame for the dispersed phase computations. The Euler–Lagrange method can also be used for dense dispersed flows, however it is usually computationally too costly, because of the huge number of particles that have to be resolved [2].

In the Euler–Lagrange approach of the two-phase flow modeling, the particles‘ motion is computed in the Lagrangian frame by the direct use of Newton’s laws, with momentum and energy transfer models taking into account the particle–fluid interactions [3]. The computationally most affordable approach is description of a particle as a rigid sphere, that interacts with the fluid phase, but at the same time also occupies the same volume as the fluid. As the particle size is in general much smaller than the elements of the computational grid, used for the numerical solution of the Eulerian part of the problem, the interaction of both phases can be modeled by a point source approach [3]. The resulting Lagrangian particle tracking has a superior spatial accuracy, and allows different phenomena to be modeled and computed accurately, e.g. heat and mass transfer from the particles or accurate incorporation of drag and lift forces. In general, the transport phenomena between the phases influence the state of both phases, however, if the impact of one phase on the other is weak, it can be neglected in the computational model, leading to so called one-way coupling between the phases. Conversely, the mutual influence on both phases is covered by the two-way coupling algorithms.

Solving the one-way coupled problem generally requires the availability of the velocity, temperature and moisture concentration in the fluid phase at the current location of the particle, which is then used in computation of the particle drying kinetics. In drying applications,

* Corresponding author.
E-mail address: timi.gomboc@um.si (T. Gomboc).

https://doi.org/10.1016/j.enganabound.2023.01.042
Received 14 December 2021; Received in revised form 10 December 2022; Accepted 31 January 2023

the moisture partial pressure difference between the fluid phase and the particle presents the driving force for moisture evaporation, which leads to a change in moisture concentration field in the fluid phase. As this change alters the mass transfer driving force, a two-way coupling has to be implemented in order not to loose accuracy of computed drying rates of particles. This calls for an accurate representation of the heat and mass flows from the particles at the level of the fluid, which leads to a correct distribution of the flows to the computational nodes. The particles' feedback to the continuous phase is solved using different mathematical approximations. Verhnjak et al. [4] published a novel computational approach for the two-way coupled simulation of heat transfer from point sources that can be used in Subdomain Boundary Domain Integral Method, used for solution of the continuous phase. The approach is based on the point particle approximation and takes advantage of the Dirac delta distribution properties when mapping the dispersed phase impact onto the fluid phase. The mapping is extremely accurate except for the case of particle's position in close proximity of the mesh nodes, where the Dirac delta distribution is singular. The problem was fixed with the proposed hybrid BEM-PIC (Particle-In-Cell) model, that is used in these regions, which typically occupy only 1%–3% of the computational domain. As the BEM based point particle mapping outperforms other traditional models [5,6] in the 97%–99% of the computational domain, the model is extended here to the drying case, i.e. particles (i.e. sources) moving in the flow and exchanging heat and mass with the fluid phase.

In general, the drying process is a two-way interaction of momentum, heat and mass transfer between the dispersed particles and the drying fluid. In drying of dispersed phase, one-way coupling can used to account for the impact of the drying fluid momentum on the dispersed phase [7]. In the case of drying, two-way coupling is needed, as the conditions in the drying fluid directly influence the heat and mass exchange with the particles, which in turn directly affect the local conditions within the drying air. The two-way coupling leads to more accurate calculation of the particle drying time [8], which is the most important engineering parameter in drying [9,10]. Although the present work focuses on the development of a point source model for the drying fluid, computation of particle kinetics has to be included as well. Here, we refer to the work of Sagadin and Hribersek [11] where a multistage spray drying model of zeolite 4 A particles was developed. Additionally, Gomboc et al. [12] published a paper that extends the model in [11] with the heat transfer inside the particle solved using BEM, by transforming a 3D problem into a quasi 1D case, with the time dependent solution leading to calculation of energy and mass sources for the use in the two-way coupling numerical simulation of the drying process.

The paper is organized as follows. Section 2 describes the mathematical model of the two-way coupling model for heat and mass transfer between the continuous phase and the dispersed phase. A description of the BEM implementation in developing the final numerical model is presented in Section 3. Computational examples are presented in Section 4, while the results and discussion are presented in Section 5. The paper ends with the Conclusion and Acknowledgments.

2. Mathematical model

The conjugate heat and mass transfer model between the continuous and dispersed phase requires separate computation of transport phenomena at the continuous (fluid) level as well as at the particle level. As the paper is focused on the heat and mass transfer equations for the fluid flow and contribution of the drying particles to this flow, in the following, the derivation of Boundary Element based model of moving point sources in the fluid phase will be presented, with the extension to the Boundary Element based model of drying at the particle (point source) level.

2.1. Heat and mass transfer in the continuous phase

In order to accurately compute the drying rates for the moving particles, temperature as well as moisture concentration values at locations of particles have to be known, which requires the solution of Navier–Stokes equations with heat and mass transfer included in the system of equations. The BEM based numerical model for the solution of Navier–Stokes equations for the fluid flow simulation is described in more detail in the work of Ravnik et al. [13,14], with extension to solving the heat and mass conservation laws using BEM. Therefore, in this section, we will be focusing only on the numerical solution of heat and mass conservation equations, which will include the source terms arising from the drying of particles.

As described, the drying process includes the heat and mass transfer between the dispersed particles and the drying air. Heat from the drying air transfers to the dispersed particles, where drying takes place, inducing a heat sink in the drying air. Conversely, the evaporated moisture flows from the particles to the drying air, inducing the moisture source in the fluid phase. Consequently, a change in local drying conditions give rise to differences in drying kinetics of the particles [12].

Heat transfer in the drying air can be accounted for by the conservation of energy as:

$$\rho^* c_p^* \frac{\partial T^*}{\partial t^*} + \left(\vec{v}^* \cdot \vec{\nabla}\right) T^* = \lambda^* \vec{\nabla}^2 T^* + I_T^*, \tag{1}$$

where ρ^* represent density, c_p^* represent specific heat, T^* temperature, t^* time, $\vec{v}^*$ velocity, λ^* thermal conductivity, $\vec{\nabla}$ represents the nabla operator and I_T^* heat sink. * represents the dimensional form, and has been introduced due to the clear writing of the non-dimensional form below.

Mass transfer in the drying air can be accounted for by the conservation of mass of species as:

$$\frac{\partial C^*}{\partial t^*} + \left(\vec{v}^* \cdot \vec{\nabla}\right) C^* = \vec{\nabla} \cdot \left(D^* \vec{\nabla} C^*\right) + I_C^*, \tag{2}$$

where C^* represents moisture concentration, D^* the moisture diffusion coefficient in air and I_C^* the moisture source.

In spray drying applications the drying particle size is between 50 μm and 300 μm [15]. In that case, when we deal with small particles which are usually much smaller than the computational mesh element size and their Stokes number values are much smaller than one, particles can be approximated as points and their interaction with the fluid phase as a point source type interaction. The heat sink can be expressed as [4]:

$$I_T^* = \sum_l Q_{T,l}^* \delta\left(\vec{r}^*, \vec{p}_l^*\right), \tag{3}$$

where $Q_{T,l}^*$ represents the heat power of a single particle, δ is the Dirac delta distribution, $\vec{r}^*$ represents the arbitrary position vector, $\vec{p}_l^*$ represents the particle position, and summation the sum of all particles. The Dirac delta distribution gives a mathematically exact expression for the point-wise property of the particles. Similar to the heat source the mass source can be expressed as:

$$I_C^* = \sum_l Q_{C,l}^* \delta\left(\vec{r}^* - \vec{p}_l^*\right), \tag{4}$$

where $Q_{C,l}^*$ represents the mass power of the individual particle l.

Both governing equations Eqs. (1) and (2) are cast into their non-dimensional forms using the following definitions:

$$t = \frac{v_0^* t^*}{L^*}, \quad \lambda = \frac{\lambda^*}{\lambda_0^*}, \quad \rho = \frac{\rho^*}{\rho_0^*}, \quad C = \frac{C^*}{C_0^*}, \quad I_T = \frac{I_T^*}{I_{T_0}^*},$$
$$T = \frac{T^* - T_0^*}{\Delta T^*}, \quad v = \frac{v^*}{v_0^*}, \quad c_p = \frac{c_p^*}{c_{p_0}^*}, \quad I_C = \frac{I_C^*}{I_{C_0}^*}, \tag{5}$$

where v_0^*, λ_0^*, ρ_0^*, c_{p0}^*, T_0^*, C_0^*, L^*, I_{T0}^* and I_{C0}^* represent their characteristic counterparts.

The non-dimensional forms of Eqs. (1) and (2) together with the heat and mass sink definitions (3) and (4) now read as:

$$\frac{\partial T}{\partial t}+\left(\vec{v}\cdot\vec{\nabla}\right)T=\frac{1}{RePr}\nabla^2 T+\sum_l \vartheta_{T,l}\delta\left(\vec{r}-\vec{p}_l\right), \tag{6}$$

where the heat source is written as $\vartheta_T = I_0^* L^*/(\Delta T^* v_0^* \rho_0^* c_0^*)$, with Re and Pr representing the Reynolds and Prandtl numbers, and:

$$\frac{\partial C}{\partial t}+\left(\vec{v}\cdot\vec{\nabla}\right)C=\frac{1}{ScRe}\nabla^2 C+\sum_l \vartheta_{C,l}\delta\left(\vec{r}-\vec{p}_l\right), \tag{7}$$

where the mass source is written as $\vartheta_C = I_{C0}^* L^*/(C_0^* v_0^*)$ and Sc represent the Schmidt number.

The point source model is based on the properties of the Dirac delta distribution, which is singular at the exact location of the particle. Generally, all the numerical approaches approximate the Diract delta distribution by means of some smooth function, which resembles the Dirac delta properties more or less accurately [16,17]. In the case of Boundary Element Methods, the point source in an integral equation can be evaluated analytically, if the field point does not coincide with the source point. However, in the case when the particle (i.e. the field point) is at the source point position or very close to it, numerical problems occur. The hybrid methodology, introduced by Verhnjak et al. [4], solves this problem by implementing an approximation of the Dirac delta distribution when the field point is in close vicinity of the source point, which occurs only in a small fraction of the computational domain, typically in the range of 1%–3% Verhnjak et al. [4]. This hybrid methodology is based on the local application of the particle-in-cell (PIC) method [5], and can be expressed for the heat sink as:

$$I_T=\sum_l \frac{\vartheta_{T,l}}{V_c}, \tag{8}$$

where V_c represents a small volume of the entire domain. Similarly, we express the mass source as:

$$I_C=\sum_l \frac{\vartheta_{C,l}}{V_c}. \tag{9}$$

In the case when the Dirac delta distribution is singular or near-singular, Eqs. (6) and (7) can be rewritten to:

$$\frac{\partial T}{\partial t}+\left(\vec{v}\cdot\vec{\nabla}\right)T=\frac{1}{RePr}\nabla^2 T+\sum_l \frac{\vartheta_{T,l}}{V_c}, \tag{10}$$

$$\frac{\partial C}{\partial t}+\left(\vec{v}\cdot\vec{\nabla}\right)C=\frac{1}{ScRe}\nabla^2 C+\sum_l \frac{\vartheta_{C,l}}{V_c}, \tag{11}$$

presenting the final form used in BEM discretization process. A critical non-dimensional distance of 0.01 was used to switch between the Dirac delta distribution approach and the macroscopic PIC approach [4].

As the particles are tracked in the fluid flow, the latter has to be resolved as well. As stated before, the dilute two-phase flow case is considered here, where one-way coupling is implemented. Laminar viscous flow was simulated using the code developed in [13]. The code solves the velocity–vorticity formulation of the Navier–Stokes equations using the Boundary-Domain Integral Method. A combination of sub-domain and single domain technique is used and incompressible viscous Newtonian fluid with constant material properties is considered. Vorticity $\vec{\omega}$ is defined as the curl of the velocity $\vec{\omega}=\vec{\nabla}\times\vec{v}$. Both velocity and vorticity fields are divergence free. The viscous fluid flow is governed by the kinematics equation

$$\nabla^2\vec{v}+\vec{\nabla}\times\vec{\omega}=0, \tag{12}$$

which links the velocity and vorticity fields for every point in space and time. The kinetic aspect of the fluid flow is governed by the vorticity transport equation [4], written in the following non-dimensional form:

$$\frac{\partial\vec{\omega}}{\partial t}+(\vec{v}\cdot\vec{\nabla})\vec{\omega}=(\vec{\omega}\cdot\vec{\nabla})\vec{v}+\frac{1}{Re}\nabla^2\vec{\omega}. \tag{13}$$

Numerical solution of the fluid flow problem is reported in [13] and shall not be repeated here.

2.2. Heat and mass transfer at the particle level

As the model problem at the particle level the three-stage porous particle drying model is considered. As the first and the third drying stages are described by ordinary differential equations with respect only to time, which are solved using standard Euler or Runge–Kutta methods [11], here we will concentrate on just the second stage, which is governed by the heat transfer inside the particle and the Stefan diffusion through the dried part of the particle accounting for the mass transfer, presenting the computationally most difficult part as well as accounting for the majority of the overall drying time.

During the second stage, drying takes place inside the particle, where the moisture is evaporated at the drying front (i.e. the interface between the dried and wet part of the particle) and transferred to the outer surface of the particle by means of the Stefan diffusion [9,11]. Therefore, the particle can be divided into two regions during the second stage — the dry and the wet regions, or the dry crust and the wet core, respectively. During the drying stage, the drying front is moving as the wet core decreases in size until there is no wet region inside the particle. As the evaporation intensity at the drying front depends on the temperature, to solve the second stage, we have to solve the heat transfer inside the particle. Heat transfer inside the wet core and the dry crust can be described by the conservation of energy as:

$$\rho_o^* c_{p,o}^* \frac{\partial T_o^*}{\partial t^*}=\vec{\nabla}\cdot\left(\lambda_o^*\vec{\nabla}T_o^*\right), \tag{14}$$

where index $o=\{w,d\}$ denotes wet or dry region.

To solve the unsteady heat transfer through the dry and wet regions, we also have to impose boundary and interface conditions. Due to the particle spherical shape, we introduce a spherical coordinate system $\vec{r}=\vec{r}\,(r,\varphi,\theta)$ for simpler annotation. Heating or cooling of a particle at the outer surface is described with Robin boundary condition as:

$$\begin{aligned} &q^*=-\lambda_d^*\vec{\nabla}T_d^*\cdot\vec{n}=\alpha^*(T_g^*-T_d^*),\\ &r^*=R_p^*,\quad 0\le\varphi\le 2\pi,\quad -\pi\le\theta\le\pi, \end{aligned} \tag{15}$$

where q^* represents the heat flux, T_d^* the temperature of the dry crust, T_g^* is the temperature of the drying gas far away from the particle, α^* is the heat transfer coefficient, λ_d^* the effective heat conductivity of the dry region, $\vec{n}$ is a normal vector of the surface, and R_p^* the radius of the particle. At the interface, we impose a compatibility condition for the temperature as:

$$T_w^*=T_d^*,\qquad r^*=R_i^*,\quad 0\le\varphi\le 2\pi,\quad -\pi\le\theta\le\pi, \tag{16}$$

where T_w^* represents the temperature of the wet core, R_i^* is the interface radius, and equilibrium conditions, where evaporation of the moisture is included, as:

$$\lambda_d^*\frac{\partial T_d^*}{\partial r^*}=\lambda_w^*\frac{\partial T_w^*}{\partial r^*}+h^*\frac{\dot{m}_{f,i}^*}{A_i^*}\qquad r^*=R_i^*,\quad 0\le\varphi\le 2\pi,\quad -\pi\le\theta\le\pi \tag{17}$$

where λ_w^* represents the effective thermal conductivity of the wet core, h^* is the specific heat of evaporation, A_i^* is the interface surface area, and $\dot{m}_{f,i}^*$ the fluid vapor mass flow rate at the interface. Because the boundary conditions on the particle surface (15) are uniform in all directions and the particle is treated as homogeneous, the drying rate will also be the same in all directions.

As stated, mass transfer of vapor from the drying front to the particle surface through the dried crust is solved by using the solution of the Stefan diffusion through a porous material under the assumption of cylindrical inner channels, described by the equation [18]

$$\dot{m}_{f,i}^*=-\frac{8\pi\epsilon^\beta D_{f,d}^* M_f^* p_g^*}{\kappa^*\left(\bar{T}_d^*+\bar{T}_w^*\right)}\frac{R_p^* R_i^*}{R_p^*-R_i^*}ln\left[\frac{p_g^*-p_{f,i}^*}{p_g^*-\left(\frac{\kappa^*}{4\pi M_f^*\alpha_m^* R_p^{*2}}\dot{m}_{f,i}^*+\frac{p_{f,\infty}^*}{T_g^*}\right)T_i^*}\right], \tag{18}$$

where ε represents the porosity of the particle, β the power coefficient, M_f^* the fluid molecular weight, κ^* the universal gas constant, p_g^* the drying gas pressure, $D_{f,d}^*$ the vapor diffusion coefficient in the dry crust, $\bar{T}_d^*$ and $\bar{T}_w^*$ are the average temperature of the dry crust and the wet core, respectively, T_i^* represents the temperature at the wet core-dry crust interface, $p_{f,i}^*$ is the saturation pressure of vapor on the interface while $p_{f,\infty}^*$ represent the partial pressure of the vapor in the drying gas and α_m^* the mass transfer coefficient. The saturation pressure of the vapor depends on the temperature and is calculated from the model [11]:

$$p_{f,i}^* = \frac{e^{a_1 + a_2 T_i^* \frac{a_3}{T_i^*}}}{T_i^{*a_4}}, \tag{19}$$

while other parameters in the Eq. (18) are kept constant as well as the coefficients. Variables a_1, a_2, a_3, and a_4 in the Eq. (19) are constants. As can be seen, Eq. (18) for calculation of the mass flow rate for the evaporated fluid at the interface is non-linear and has to be solved using an iterative approach.

The change of the wet core volume is calculated using the conservation of mass written for the moisture, assuming that the wet core has a spherical shape, as:

$$\frac{\partial R_i^*}{\partial t^*} = -\frac{1}{\varepsilon \rho_f^* 4\pi R_i^{*2}} \dot{m}_{f,i}^*, \tag{20}$$

where ρ_f^* represents the fluid density.

The heat transfer problem described by Eq. (14), written for the dry and wet regions, together with boundary and interface conditions (15)–(17) was solved using the BEM, Eq. (18) has been solved using an iterative solver and Eq. (20) by using the classical Euler algorithm. The BEM derivation for the energy equation is described in detail in the work of Gomboc et al. [8].

In order to accurately compute the heat and mass source terms one needs to track all the individual particles in the fluid flow. The particle positions and velocities in the fluid flow are computed by using the Lagrangian particle tracking, which requires computation of a particle position and velocity. The equation of particle motion is given by

$$\frac{d^2\vec{p}}{dt} = \vec{a}_p(\vec{v}_p, \vec{v}), \tag{21}$$

where $\vec{p}$ is the location of the particle and $\vec{a}_p$ is its acceleration, which depends on the particle velocity $\vec{v}_p$ and on the fluid velocity $\vec{v}$. The equation for the particle acceleration is given by [19] as

$$\frac{d\vec{v}_p}{dt} = \vec{g} - \frac{\rho}{\rho_p}\vec{g} + \frac{\vec{v} - \vec{v}_p}{\tau_p}, \tag{22}$$

where ρ, ν are the fluid density and viscosity, ρ_p, d_p, τ_p are the particle density, particle diameter and $\tau_p = \rho_p d_p^2 / \rho 18\nu$ is the particle relaxation time. The terms included in Eq. (22) are gravity, buoyancy and drag. Details on numerical implementation of the Lagrangian particle tracking can be found in [20,21].

3. Numerical solution of the heat and mass transfer in the continuous phase

The subdomain BEM has been used to solve the mass and momentum equation for the fluid, as well as for the heat and mass transfer process between the porous particles and the drying air. The BEM derivation for the solution of flow kinematics Eq. (12) and vorticity transport Eq. (13) is described in detail in the works of Ravnik et al. [13,22] and will therefore be omitted here. Similarly, the numerical solution of the heat transfer with the moving front, Eqs. (14)–(17), by BEM is reported in [12]. The main aim of this paper is to describe the numerical solution of the heat and mass conservation equations described by Eqs. (6) and (7) using the subdomain BEM, with a special emphasis on the numerical treatment of the source terms.

Because both the heat and mass conservation equations are convection–diffusion type equations containing the same terms, i.e. diffusion, convection and source terms, the derivation of the subdomain BEM will be presented in a general form. The convection–diffusion equation can be written as:

$$\frac{\partial u(\vec{r},t)}{\partial t} + \left(\vec{v}\cdot\vec{\nabla}\right) u(\vec{r},t) = \frac{1}{K}\vec{\nabla}^2 u(\vec{r},t) + I(\vec{r}), \tag{23}$$

where u represents an arbitrary field function, which, in our case, can be temperature ($u = T$) or moisture concentration ($u = C$), $\vec{r}$ is an arbitrary spatial vector, K is $RePr$ for heat and $ScRe$ for mass conservation, and I is a general source term. The general governing Eq. (23) has a form of a Poisson equation, therefore the elliptic fundamental solution will be used in derivation of integral equations. The Poisson equation can be written in the following form:

$$\vec{\nabla}^2 u(\vec{r}) = K b(\vec{r}), \tag{24}$$

where $b(\vec{r})$ is a non-homogeneous term on the right hand side, following the Eq. (23):

$$b(\vec{r}) = \frac{\partial u(\vec{r})}{\partial t} + \left(\vec{v}\cdot\vec{\nabla}\right) u(\vec{r}) - I(\vec{r}). \tag{25}$$

Now we can use the integral form of Green's second identity for the Poisson Eq. (24), applying it only to one subdomain of the computational mesh, resulting in:

$$c(\vec{\xi})u(\vec{\xi}) + \int_{\Gamma_c} u(\vec{R}) q^*(\vec{\xi},\vec{R}) d\Gamma_c + \int_{\Omega_c} K b(\vec{r}) u^*(\vec{\xi},\vec{r}) d\Omega_c = \int_{\Gamma_c} q(\vec{R}) u^*(\vec{\xi},\vec{R}) d\Gamma_c, \tag{26}$$

where Ω_c represents the computational subdomain or the mesh cell, Γ_c is the mesh cell boundary, $\vec{\xi}$ is the position vector of the source point, $\vec{R}$ is the spatial vector of the cell boundary, $\vec{q} = \vec{\nabla}u \cdot \vec{n}$ represents the normal derivative of the field function, c is the free coefficient that depends on the position of the source point, and u^* and q^* are the fundamental solution and its normal derivative, respectively. The elliptical fundamental solution for 3D case is defined as [23]:

$$u^*(\vec{\xi},\vec{r}) = \frac{1}{4\pi d(\vec{\xi},\vec{r})}, \tag{27}$$

where $d(\vec{\xi},\vec{r})$ represents the distance between the arbitrary field and the source point; $d(\vec{\xi},\vec{r}) = \left\|\vec{\xi} - \vec{r}\right\|$. The normal derivative of the fundamental solution is defined by the equation:

$$q^*(\vec{\xi},\vec{R}) = \vec{\nabla}u^*(\vec{\xi},\vec{R}) \cdot \vec{n}, \tag{28}$$

where $\vec{n}$ represents the surface normal vector.

The Eq. (26) can be rewritten using the expression (25) for the non-homogeneous term as:

$$c(\vec{\xi})u(\vec{\xi}) + \int_{\Gamma_c} u(\vec{R}) q^*(\vec{\xi},\vec{R}) d\Gamma_c + \int_{\Omega_c} K \frac{\partial u(\vec{r})}{\partial t} u^*(\vec{\xi},\vec{r}) d\Omega_c + \int_{\Omega_c} K \left(\vec{v}\cdot\vec{\nabla}\right) u(\vec{r}) u^*(\vec{\xi},\vec{r}) d\Omega_c = \int_{\Gamma_c} q(\vec{R}) u^*(\vec{\xi},\vec{R}) d\Gamma_c + \int_{\Omega_c} K I(\vec{r}) u^*(\vec{\xi},\vec{r}) d\Omega_c, \tag{29}$$

A second-order equidistant finite difference (FD) scheme is used to approximate the time derivative in the Eq. (29):

$$\frac{\partial u}{\partial t} \approx \frac{3u^t - 4u^{t-1} + u^{t-2}}{2\Delta t}, \tag{30}$$

where indices t, $t-1$, $t-2$ represent different time steps, and Δt is the time difference between two time steps.

Due to the solenoidality of the velocity fields $(\vec{v}\cdot\vec{\nabla})u = \vec{\nabla}\cdot(\vec{v}u)$, the domain integral in Eq. (29) can be transformed to:

$$\int_{\Omega_c} \left(\vec{v}\cdot\vec{\nabla}\right) u(\vec{r}) u^*(\vec{\xi},\vec{r}) d\Omega_c = \int_{\Omega_c} \vec{\nabla}\cdot(\vec{v}u(\vec{r})) u^*(\vec{\xi},\vec{r}) d\Omega_c. \tag{31}$$

With the use of the algebraic relation $\vec{\nabla}\cdot(u^*\vec{v}u) = u^*\vec{\nabla}\cdot(\vec{v}u) + \vec{v}u\cdot\vec{\nabla}u^*$ we can split the domain integral in Eq. (31) into two parts:

$$\int_{\Omega_c}\vec{\nabla}\cdot(\vec{v}u(\vec{r}))u^*(\vec{\xi},\vec{r})d\Omega_c = \int_{\Gamma_c}\vec{n}\cdot(u^*(\vec{\xi},\vec{r})\vec{v}u(\vec{r}))d\Gamma_c - \int_{\Omega_c}(\vec{v}u(\vec{r}))\cdot\vec{\nabla}u^*(\vec{\xi},\vec{r})d\Omega_c. \tag{32}$$

We managed to transform one part of the domain integral to the boundary integral. Using the expressions (30) and (32) and using a fully implicit time scheme $u = u^t$, $q = q^t$ in Eq. (29), we can rewrite the final integral form of the transport equation as:

$$\begin{aligned} &c(\vec{\xi})u^t(\vec{\xi}) + \int_{\Gamma_c}u^t(\vec{R})q^*(\vec{\xi},\vec{R})d\Gamma_c \\ &+\int_{\Omega_c}K\left(\alpha_1u^t(\vec{r}) + \alpha_2u^{t-1}(\vec{r}) + \alpha_3u^{t-2}(\vec{r})\right)u^*(\vec{\xi},\vec{r})d\Omega_c + \\ &\int_{\Gamma_c}K\vec{n}\cdot(u^*(\vec{\xi},\vec{r})\vec{v}u^t(\vec{r}))d\Gamma_c - \int_{\Omega_c}K(\vec{v}u^t(\vec{r}))\cdot\vec{\nabla}u^*(\vec{\xi},\vec{r})d\Omega_c = \\ &\int_{\Gamma_c}q^t(\vec{R})u^*(\vec{\xi},\vec{R})d\Gamma_c + \int_{\Omega_c}KI(\vec{r})u^*(\vec{\xi},\vec{r})d\Omega_c, \end{aligned} \tag{33}$$

where coefficients α_1, α_2 and α_3 are $\alpha_1 = 3/(2\Delta t)$, $\alpha_2 = -2/\Delta t$ and $\alpha_3 = 1/(2\Delta t)$.

Each integral has to be computed for solving the integral Eq. (33). In order to do this the computational domain is discretized and geometry and field functions are interpolated. The quadratic interpolation functions were used for the field function u inside the cells, $u = \sum_i \phi_i u_i$, as well as on the cell boundary, $u = \sum_j \varphi_j u_j$, while the non-continuous linear interpolation was used for the field function q on the cell boundary, $q = \sum_k \kappa_k q_k$ [24].

The only exception here is the evaluation of the domain integral containing the source term. As stated before, the point particle approach is used and the domain integral of the source term can be solved analytically by using the properties of the elliptic fundamental solution [4]:

$$\int_{\Omega_c}KI(\vec{r})u^*(\vec{\xi},\vec{r})d\Omega_c = \int_{\Omega_c}\sum_l K\vartheta_l\delta\left(\vec{r},\vec{p}_l\right)u^*(\vec{\xi},\vec{r})d\Omega_c = \sum_l K\vartheta_l u^*(\vec{\xi},\vec{p}_l), \tag{34}$$

where index l represents an individual particle, and summation represents the sum over all of the particles inside the mesh cell Ω_c. As evident, the integral is now represented by a simple multiplication of the value of the fundamental solution at the particle location and the source intensity. When the source point $\vec{\xi}$ is close to the position of the individual particle, $\vec{p}_l$, the singularity of the fundamental solution $u^*(\vec{\xi},\vec{p}_l)$ leads to numerical problems. In this case the source term is approximated using the PIC approach that is described in detail in the work of Verhnjak et al. [4], and the domain integral becomes:

$$\int_{\Omega_c}KI(\vec{r})u^*(\vec{\xi},\vec{r})d\Omega_c = \int_{\Omega_c}\sum_l K\frac{\vartheta_l}{V_c}u^*(\vec{\xi},\vec{r})d\Omega_c = \sum_l K\frac{\vartheta_l}{V_c}\left[\frac{2}{3}\right]^3, \tag{35}$$

where V_c represents the volume of the mesh cell. By applying interpolation functions in the Eq. (33) one can write:

$$\begin{aligned} &c(\vec{\xi})u^t(\vec{\xi}) + \sum_j u_j^t\int_{\Gamma_c}\varphi_j q^*(\vec{\xi},\vec{R})d\Gamma_c \\ &+\sum_i K\left(\alpha_1u_i^t + \alpha_2u_i^{t-1} + \alpha_3u_i^{t-2}\right)\int_{\Omega_c}\phi_i u^*(\vec{\xi},\vec{r})d\Omega_c + \\ &\sum_j K\vec{v}u_j^t\int_{\Gamma_c}\varphi_j\vec{n}u^*(\vec{\xi},\vec{r})d\Gamma_c - \sum_i K\vec{v}u_i^t\int_{\Omega_c}\phi_i\vec{\nabla}u^*(\vec{\xi},\vec{r})d\Omega_c = \\ &\sum_k q_k^t\int_{\Gamma_c}\kappa_k u^*(\vec{\xi},\vec{R})d\Gamma_c + i_c, \end{aligned} \tag{36}$$

where i_c represents the contribution of the source terms to the mesh cell, depending on the distance between the source point and the particle's position, calculated using Eqs. (34) or (35). Finally, by calculating the integrals, Eq. (37), and by applying a source point to each node of the mesh cell, we obtain the matrix form of the transport Eq. (38):

$$\begin{aligned} &[H_c] = \int_{\Gamma_c}\varphi_j q^*(\vec{\xi},\vec{R})d\Gamma_c, \qquad [G_c] = \int_{\Gamma_c}\kappa_k u^*(\vec{\xi},\vec{R})d\Gamma_c \\ &[S_c] = \int_{\Omega_c}\phi_i u^*(\vec{\xi},\vec{r})d\Omega_c, \\ &[\vec{A}_{\vec{c}}] = \int_{\Gamma_c}\varphi_j\vec{n}u^*(\vec{\xi},\vec{r})d\Gamma_c, \qquad [\vec{D}_{\vec{c}}] = \int_{\Omega_c}\phi_i\vec{\nabla}u^*(\vec{\xi},\vec{r})d\Omega_c, \end{aligned} \tag{37}$$

$$\begin{aligned} [H_c]\left\{u^t\right\} =& [G_c]\left\{q^t\right\} - K[S_c]\left\{\alpha_1u^t + \alpha_2u^{t-1} + \alpha_3u^{t-2}\right\} \\ &- K[\vec{A}_{\vec{c}}]\left\{\vec{v}u^t\right\} + K[\vec{D}_{\vec{c}}]\left\{\vec{v}u^t\right\} + \left\{i_c\right\} \end{aligned} \tag{38}$$

The derived numerical scheme is applied to each mesh cell in the computational domain, and combined through the compatibility and equilibrium conditions [12] on the adjoining cell's boundary to a global system of linear equations that has the same form as Eq. (38). Based on the boundary conditions used for the problem, the global system of linear equations can be transformed to a general form $[A]\left\{u^t\right\} = \{b\}$, where $[A]$ represents the system matrix and $\{b\}$ the known vector on the right hand side. The resulting system is sparse, but due to its overdetermination it is solved by means of an iterative least square solver [24].

The global algorithm for solving the problem of porous particles drying in a fluid flow, including a model of conjugate heat and mass transfer between the particles and the fluid flow, based on the application of BEM based methods, can now be summarized as:

ALGORITHM 1

(1) Initialize of Time loop.
(2) Computation of fluid flow by solving Eqs. (12) and (13).
(3) Computation of new particles positions by solving Eqs. (21) and (22).
(4) Interpolation of temperature and moisture concentration values to the particle position's
(5) Heat and mass transfer computation of the second stage of porous particle drying by applying local temperature and moisture concentration values at all particle position's:
   - For each particle: computation of particle mass flux I_C representing the moisture source in the drying air, by using Eq. (15).
   - For each particle: computation of particle heat flux I_T representing the heat sink in the drying air, by using Eq. (18).
(6) Solution of the heat conservation equation for the drying air temperature based on Eq. (38), where heat sinks for all particles in computational domain are taken into account.
(7) Solution of the moisture mass conservation equation for the drying air concentration based on Eq. (38), where mass sources from all particles in the computational domain are taken into account.
(8) Proceed to 2.
(9) End of Time loop.

4. Computational example

The above presented numerical model and derived BEM based computational algorithm have been used in the simulation of particles drying in flow of hot air. We considered heat and mass diffusion and heat and mass convection from the particles into the air flow. The two-way coupling BEM based algorithm for the case of heat transfer was validated in the [4], whereas the BEM based numerical model of a single particle drying was validated in [12], so additional validation of the developed computational Algorithm 1 is omitted here.

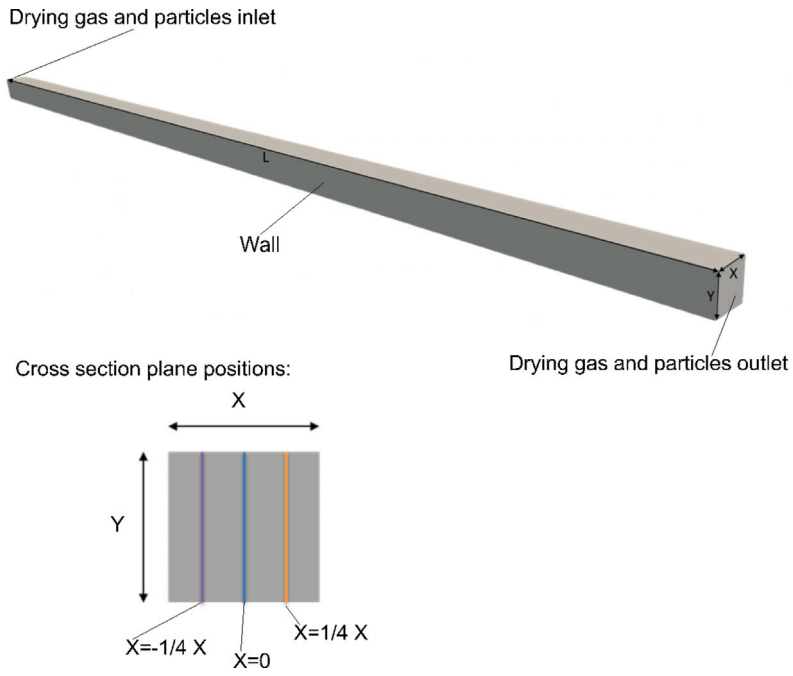

Fig. 1. Geometry of the dryer with three selected cross sections for the presentation of computed flow field values.

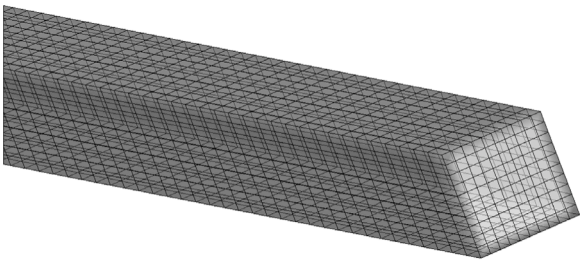

Fig. 2. Computational mesh.

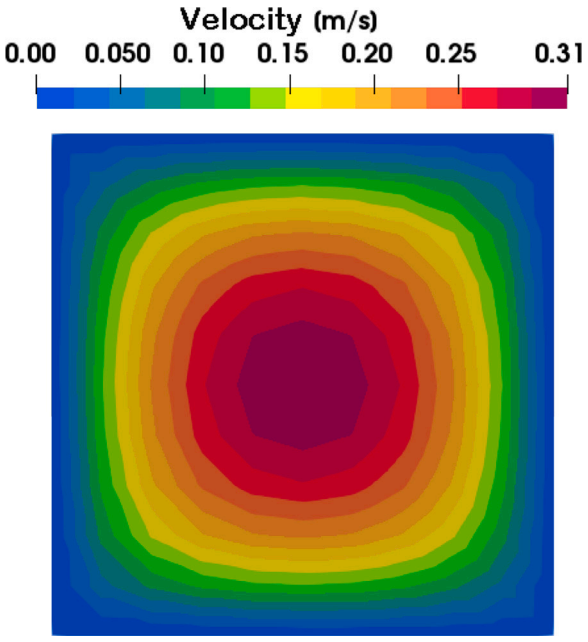

Fig. 3. Air velocity profile in drying chamber.

With respect to the case set-up, the particles had a uniform size of 100 μm, which enabled an easy and effective assessment of the effect of the two-way coupling on particle drying kinetics. Two cases were considered with different numbers of particles in the computational domain. In the first case, 1000 wet particles were used, and in the second case 10,000 particles. Regarding the different particles' positions in the computational domain, two-way coupling between the particles and the fluid was used together with a parallel computation of the drying process in the particles. The particles were set out to different local boundary conditions, which led to differences in temperature and moisture concentration conditions along each particle's trajectory, which were finally statistically analyzed.

For the drying chamber we used squared pipe geometry with the length of $L = 2000$ mm and with a side length $X = Y = 15$ mm, so the dimensionless domain size was $X = Y = 1$ and $L = 133.3$. The geometry, with boundary condition positions and positions of cross-section planes, which was used for result presentations are represented in Fig. 1. The computational domain was discretized with 7000 quadratic hexahedral elements, which represents 62,181 computational nodes. One section of the computational mesh is represented in Fig. 2.

As the drying medium the hot air was selected with an average velocity at the inlet of $v_g = 0.15$ m/s. The Reynolds number for this computational example was $Re = 76.0$, with the laminar flow profile prescribed at the inlet, shown in Fig. 3. The inlet velocity profile was calculated based on the Chen analytical solution [25]. The Schmidt and Prandtl number values were set to 1.0. In both computational cases all particles were positioned randomly at the inlet surface at the zero simulation time.

As the species mass conservation equation for the fluid phase was written for the moisture concentration, the following relation are needed in order to express the concentration with drying air humidity. First, the absolute humidity is written as the ratio between the humidity mass in the air and the dry air mass:

$$X = \frac{m_w}{m_g}, \tag{39}$$

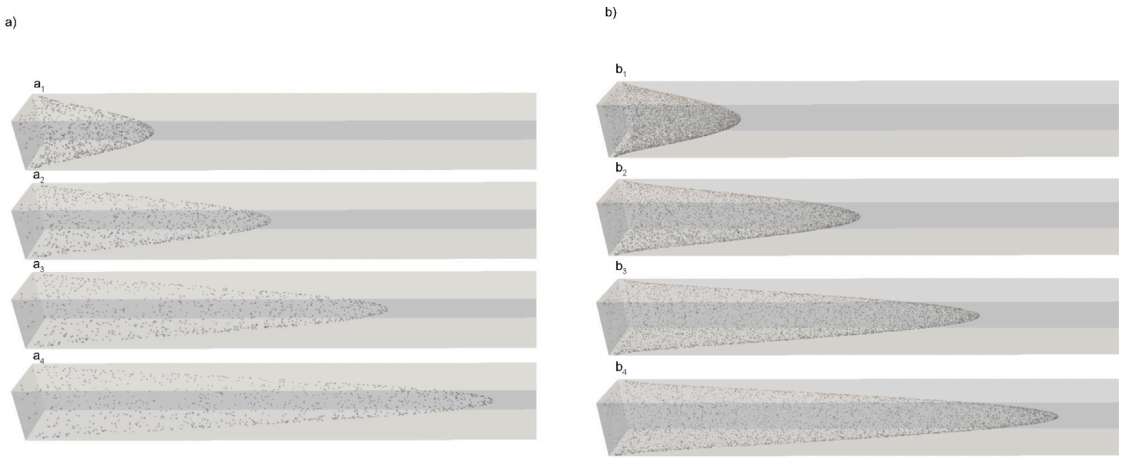

Fig. 4. Particles positions in the drying chamber at four different times: a_1 and b_1: 0.15 s, a_2 and b_2: 0.30 s, a_3 and b_3: 0.45 s and a_4 and b_4: 0.60 s.

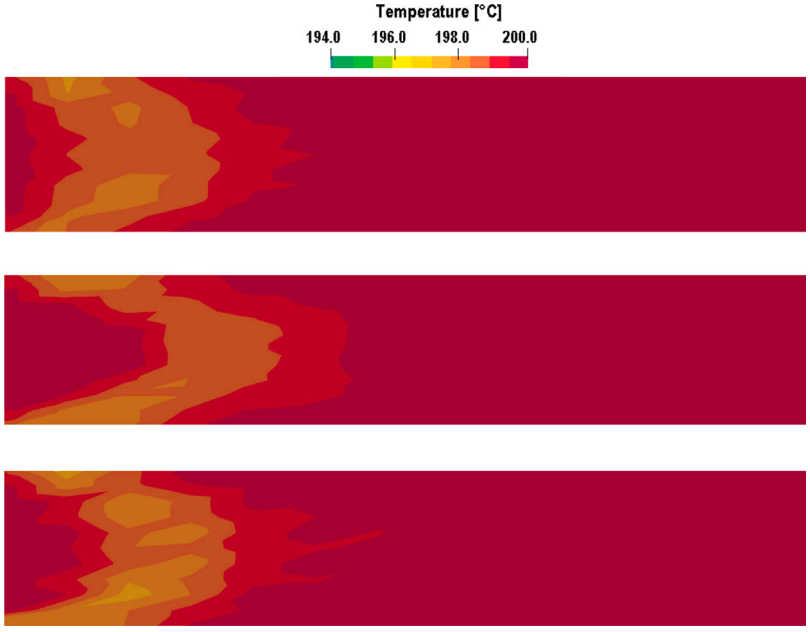

Fig. 5. Temperature field inside the drying chamber at three different cross section planes (see Fig. 1) after drying time of 0.15 s (a1 in Fig. 4).

where m_w represents the humidity mass, and m_g the dry air mass. The relation between the humidity mass fraction and air humidity can be expressed as:

$$\xi_w = \frac{m_w}{m_{hg}} = \frac{m_w}{m_w + m_g} \rightarrow \xi_w = \frac{X}{1+X} \tag{40}$$

where m_{hg} represents the mass of humid air. The relation between the mass concentration C, the mass fraction and the absolute humidity is then expressed as:

$$C = \frac{m_w}{V_{hg}} = \xi_w \rho_{hg}, \tag{41}$$

where V_{hg} represents the volume of humid air and ρ_{hg} the density of the humid air. In the particle frame, the humidity X_p of the dried particle is represented as the relation between mass of water and dry material mass:

$$X_p = \frac{m_v}{m_d}, \tag{42}$$

where m_w represents the mass of water in a particle and m_d the mass of dry particle material.

The inlet temperature of the particles was set to $T_p = 20$ °C. The drying air temperature at the inlet was set to $T_g = 200$ °C, and its absolute humidity to $X = 0.02$ kg/kg. The initial temperature and humidity field of the fluid phase were homogeneous in the whole computational domain, whereas the flow field was obtained as the solution of the steady-state simulation, and was kept constant during the drying computation, as only a one-way coupling in the case of the momentum transfer was considered. The simulation time step for the drying case was set to $\Delta t = 0.001$ s. The following material properties were used for the particles‘ drying kinetics calculation: Thermal conductivity of the wet material $\lambda_w = 0.508\ \frac{W}{mK}$, thermal conductivity of the dry material $\lambda_d = 0.0512\ \frac{W}{mK}$, porosity $\epsilon = 0.86$, wet material specific heat $c_w = 3.835$ kJ/kgK, dry material specific heat $c_d = 1.129$ kJ/kgK, initial moisture content $X_p = 0.85$ kg/kg, density $\rho_p = 1007$ kg/m^3.

5. Results and discussion

In this Section, the simulation results of the two-way coupling model between particles and air flow are presented for the two cases with different numbers of particles in the computational domain, as

Fig. 6. Humidity field inside the drying chamber at three different cross section planes (see Fig. 1) after drying time of 0.15 s.

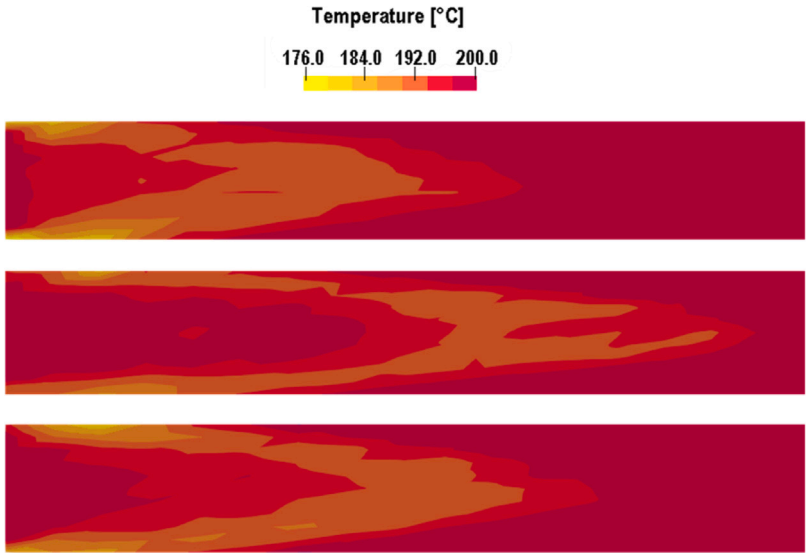

Fig. 7. Temperature field inside the drying chamber at three different cross section planes 1 after drying time of 0.3 s (a1 in Fig. 4).

discussed in the previous Section. In Fig. 4 the computed positions of particles at different time instants inside the drying chamber are presented. Because particles were introduced into the computational domain at random positions at the inlet plane where a fully developed flow is prescribed, they moved with different velocities and reached different locations after a certain time, as is shown in Fig. 4. As evident, the laminar velocity profile leads to increased penetration lengths for the particles, positioned at the inlet near the center of the channel, with respect to the particles positioned near the chamber wall.

Because at the inlet the particles have a lower temperature than the drying air, heat is transferred from the drying air to the particles, which enables a sustainable moisture evaporation process within the particles. A result is a local cooling of the fluid, observed already in the case of 1000 particles, as evident from Fig. 5, showing the conditions in the drying chamber after the drying time of 0.15 s.

Similarly to the temperature field, Fig. 6 shows the humidity field in the fluid phase, where we can see a local increase in the humidity values, a result of the moisture evaporation within the particles and its diffusion to the particle surface, where it acts as a water vapor mass source in the drying air.

The 1000 particles case inside the drying chamber represents relatively low particle density case and the effect of the particles on the drying air is small. A much more intensive changes can be observed in Fig. 7 where the temperature field in the drying chamber for the case of 10,000 particles is shown. It is interesting to observe lower temperatures in the cross sections near the solid wall (Fig. 7) together with higher humidity values (Fig. 8), which is a result of longer residence times of the particles in this region due to lower fluid velocities with respect to the conditions in the bulk of the flow. The same influence on the temperature and humidity field can also be observed in other

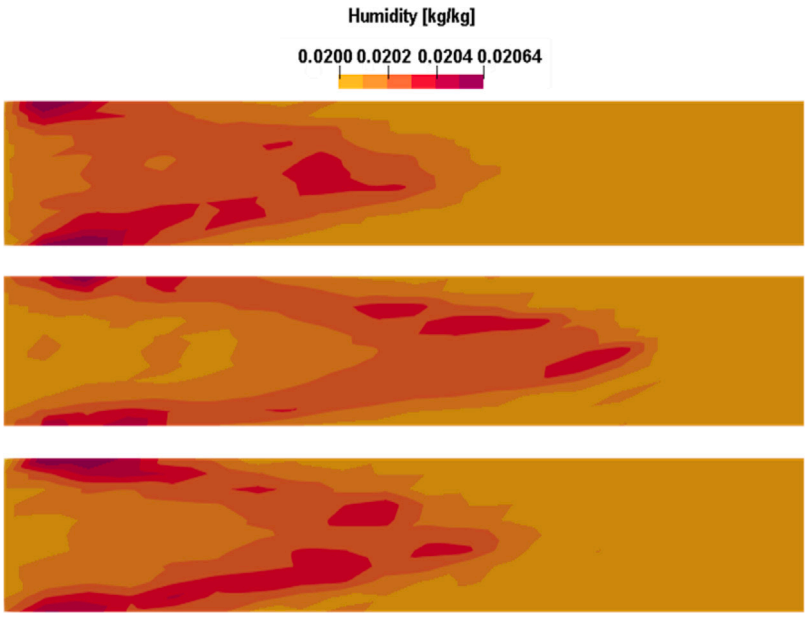

Fig. 8. Humidity field inside the drying chamber at three different cross section planes 1 after drying time of 0.3 s.

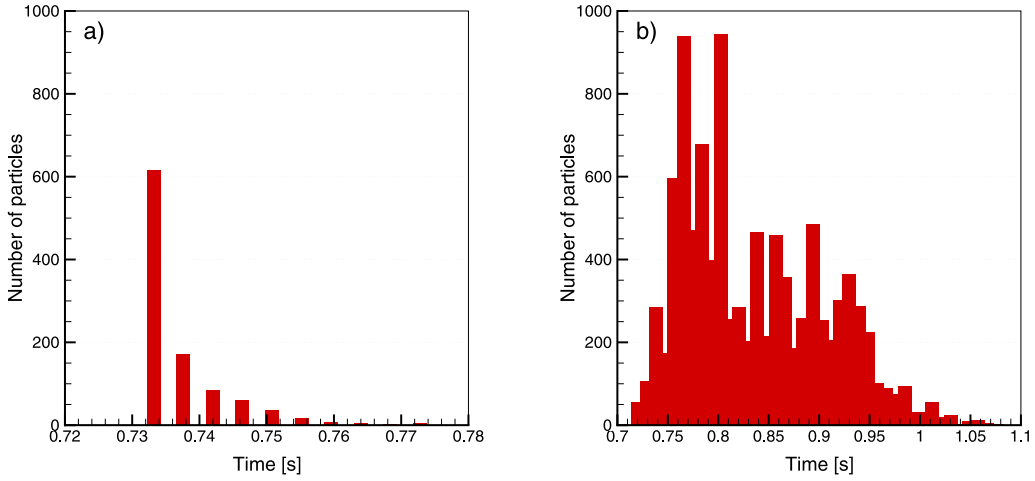

Fig. 9. Particles drying time a) Case 1 (1000 particles) b) Case 2 (10,000 particles).

near wall regions in the drying chamber. Due to the random positioning of the particles at the inlet the local temperature as well as humidity conditions at particle positions and in their wake also exhibit a certain amount of local oscillations, introducing the effect of randomness to the drying of transported porous particles.

From the engineering point of view, we usually want to determine the average required particle residence time in the drying chamber in order to achieve the desired drying quality of the products. To achieve a complete drying, the particle residence time within the chamber should be larger than its drying time. In this respect, one usually considers constant drying conditions, which would in our case correspond to the one-way heat and mass transfer coupling. When the one-way coupling is considered, all the particles are dry within 0.709s, regardless of their position or number density in the channel, as there is no influence of the particles on the temperature and humidity field in the drying air. When the two-way coupling is taken into account, the drying time for all the particles increases, as the heat and mass transfer two-way coupling directly affects the local drying conditions lading to different drying kinetics for individual particles. In Fig. 9 the histogram of drying times for the case with 1000 particles is presented. The average drying time for the 1000 particles has increased to 0.737 s, although the difference in drying times between the particles is not significant. In the case with 10,000 particles the drying time further increased to 0.836 s, with a much more pronounced drying time differences between the particles (see Fig. 9 right). The same conclusions can be made when we observe the particle average temperature, presented in Fig. 10 for the time instant of 0.5 s, and the particle humidity X_p, presented in Fig. 11 for the same 0.5 s. In the latter case, the one-way coupling model predicts the average temperature of the particles as 97.35 °C, while the average temperatures in the two-way coupling cases were 96.86 °C (Case 1) and 94.66 °C (Case 2).

6. Conclusions

In this paper a BEM based numerical model for the two-way heat and mass transfer coupling in the Euler–Lagrange resolved two-phase flows, with drying of porous particles resolved at the particle level, was presented. As point source model was used for the interaction model between the continuous and dispersed phases, its numerical implementation in the framework of BEM based solution of heat and humidity conservation in the fluid phase was based on the direct implementation of the Dirac delta distribution, which leads to exact computation of

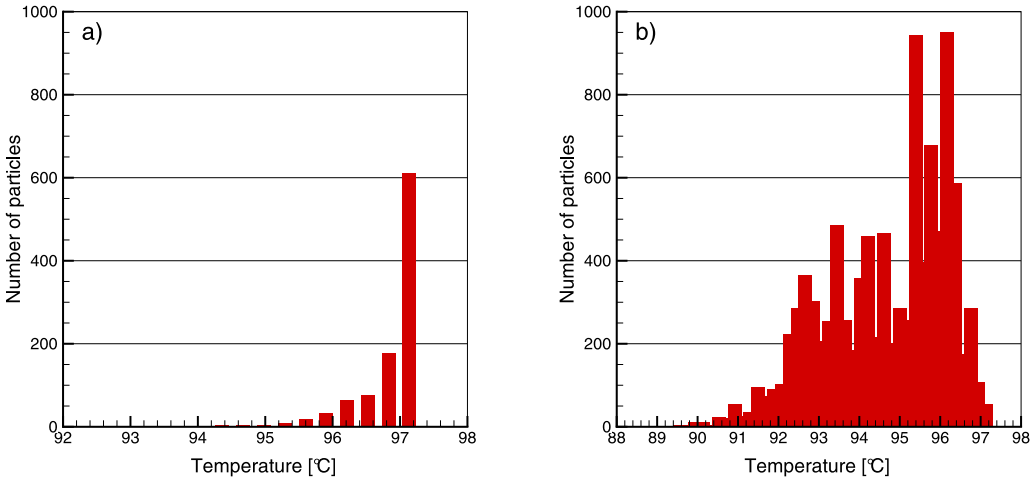

Fig. 10. Temperature of the particles after 0.5 s drying time; (a) Case 1 (1000 particles) (b) Case 2 (10,000 particles).

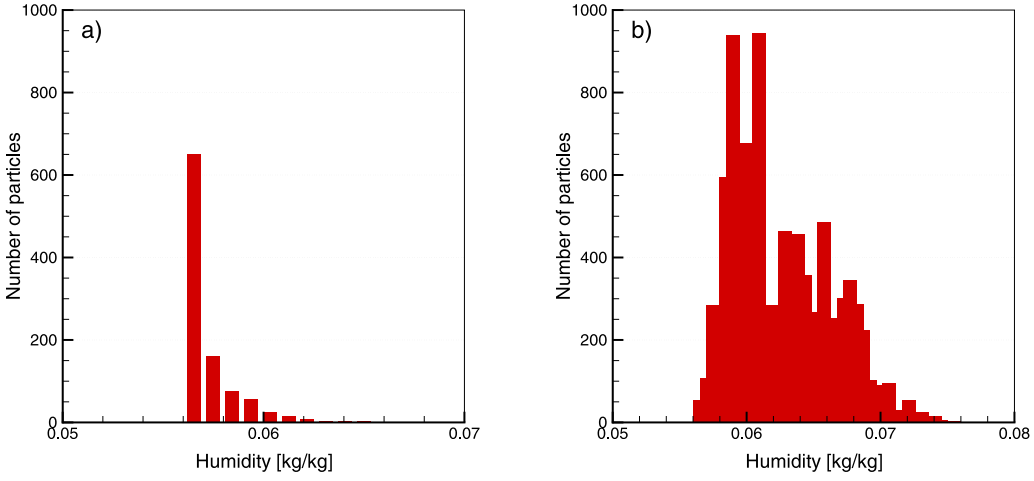

Fig. 11. Humidity of the particles after 0.5 s drying time; (a) Case 1 (1000 particles) (b) Case 2 (10,000 particles).

the point source impact on the surrounding computational nodes. The derived two-way coupling between the particles and the fluid leads to numerically very accurate evaluation of the impact of heat and mass point sources, originating from the particle level phenomena. The only exception presents the case when the point source is in close proximity to the source point, where due to singularity of the fundamental solution an approximation of the Dirac Delta distribution has to be applied, in our case in form of the Particle-in-cell approach. Two cases of drying of porous particles in a simple narrow drying channel were computed as a test example, with different numbers of particles traveling through the channel and exchanging heat and mass with the fluid phase. The computational results show, that the presented BEM based two-way coupling model is capable of generating high quality computational results and can be seen as a promising new computational tool in two-way coupled multiphase flows.

Declaration of competing interest

The authors declare that they have no known competing financial interests or personal relationships that could have appeared to influence the work reported in this paper.

Data availability

Data will be made available on request.

Acknowledgments

The authors wish to thank the Slovenian Research Agency (ARRS) for the financial support in the framework of the Program P2-0196 Research in Power, Process, and Environmental Engineering.

References

[1] Enwald H, Peirano E, Almstedt A-E. Eulerian two-phase flow theory applied to fluidization. Int J Multiph Flow 1996;22:21–66.
[2] Zhou L, Yu Y, Cai F, Zeng Z. Two-phase turbulence models for simulating dense gas–particle flows. Particuology 2014;16:100–7.
[3] Crowe C, Sommerfeld M, Tsuji Y. Multiphase flows with droplets and particles. CRC Press; 1998.
[4] Verhnjak O, Hriberšek M, Steinmann P, Ravnik J. A novel two-way coupling model for Euler-Lagrange simulations of multiphase flow. Eng Anal Bound Elem 2020;119:119–32.
[5] Harlow FH. Hydrodynamic problems involving large fluid distortions. J ACM 1957;4(2):137–42.
[6] Balachandar S, Eaton JK. Turbulent dispersed multiphase flow. Annu Rev Fluid Mech 2010;42:111–33.
[7] Benra F-K, Dohmen HJ, Pei J, Schuster S, Wan B. A comparison of one-way and two-way coupling methods for numerical analysis of fluid-structure interactions. J Appl Math 2011;2011.
[8] Gomboc T, Iljaž J, Ravnik J, Hriberšek M. Spherical porous particle drying using BEM approach. Eng Anal Bound Elem 2019;108:158–67.
[9] Mezhericher M, Levy A, Borde I. Spray drying modelling based on advanced droplet drying kinetics. Chem Eng Process: Process Intensif 2010;49(11):1205–13.
[10] Kieviet FG. Modelling quality in spray drying. Technische Universiteit Eindhoven; 1997, http://dx.doi.org/10.6100/IR477431.

[11] Sagadin G, Hriberšek M. A multistage spray drying model for zeolite 4A–water suspensions in a counter-current spray dryer. Int J Heat Mass Transfer 2017;108:1220–8.
[12] Gomboc T, Iljaž J, Ravnik J, Hriberšek M. Spherical porous particle drying using BEM approach. Eng Anal Bound Elem 2019;108:158–67.
[13] Ravnik J, Škerget L, Žunič Z. Velocity–vorticity formulation for 3D natural convection in an inclined enclosure by BEM. Int J Heat Mass Transfer 2008;51(17–18):4517–27.
[14] Žunič Z, Hriberšek M, Škerget L, Ravnik J. 3-D boundary element–finite element method for velocity–vorticity formulation of the Navier–Stokes equations. Eng Anal Bound Elem 2007;31(3):259–66.
[15] Gomboc T, Zadravec M, Ilijaz J, Sagadin G, Hribersek M. Numerical model of three stage spray drying for zeolite 4A—Water suspensions coupled with CFD flow field. Int J Simul Modelling 2019;18(2):217–28.
[16] Hosseini B, Nigam N, Stockie JM. On regularizations of the Dirac delta distribution. J Comput Phys 2016;305:423–47.
[17] Strichartz RS. A guide to distribution theory and Fourier transforms. World Scientific Publishing Company; 2003.
[18] Mezhericher M, Levy A, Borde I. Theoretical drying model of single droplets containing insoluble or dissolved solids. Drying Technol 2007;25(6):1025–32.
[19] Maxey R. Equation of motion for a small rigid sphere in a nonuniform flow. Phys Fluids 1983;26(4):883–9.
[20] Ravnik J, Hriberšek M. High gradient magnetic particle separation in viscous flows by 3D BEM. Comput Mech 2013;51(4):465–74.
[21] Ravnik J, Hriberšek M, Lupše J. Lagrangian particle tracking in velocity-vorticity resolved viscous flows by subdomain BEM. J Appl Fluid Mech 2016;9(3):1533–49.
[22] Ravnik J, Škerget L, Žunič Z. Fast single domain–subdomain BEM algorithm for 3D incompressible fluid flow and heat transfer. Internat J Numer Methods Engrg 2009;77(12):1627–45.
[23] Ramšak M, Škerget L. 3D multidomain BEM for solving the Laplace equation. Eng Anal Bound Elem 2007;31(6):528–38.
[24] Iljaž J, Wrobel L, Hriberšek M, Marn J. Subdomain BEM formulations for the solution of bio-heat problems in biological tissue with melanoma lesions. Eng Anal Bound Elem 2017;83:25–42.
[25] Chen C-S. Numerical method for predicting three-dimensional steady compressible flow in long microchannels. J Micromech Microeng 2004;14(7):1091.